LoTSS Jellyfish Galaxies. IV. Enhanced star formation on the leading half of cluster galaxies and gas compression in IC3949

Roberts, I.D.; Lang, M.; Trotsenko, D.; Bemis, A.R.; Ellison, S.L.; Lin, L.; ... ; Weeren, R.J. van

The Astrophysical Journal, 941:77 (14pp), 2022 December 10 https://doi.org/10.3847/1538-4357/ac9e9f

LoTSS Jellyfish Galaxies. IV. Enhanced Star Formation on the Leading Half of Cluster Galaxies and Gas Compression in IC3949

Ian D. Roberts[1], Maojin Lang (郎茂锦)[1], Daria Trotsenko[1], Ashley R. Bemis[1], Sara L. Ellison[2], Lihwai Lin[3], Hsi-An Pan[4], Alessandro Ignesti[5], Sarah Leslie[1], and Reinout J. van Weeren[1]
[1] Leiden Observatory, Leiden University, PO Box 9513, 2300 RA Leiden, The Netherlands
[2] Department of Physics & Astronomy, University of Victoria, Finnerty Road, Victoria, BC, V8P 1A1, Canada
[3] Institute of Astronomy and Astrophysics, Academia Sinica, No. 1, Section 4, Roosevelt Road, Taipei 10617, Taiwan
[4] Department of Physics, Tamkang University, Tamsui Dist., New Taipei City 251301, Taiwan
[5] INAF- Osservatorio astronomico di Padova, Vicolo Osservatorio 5, IT-35122 Padova, Italy
Received 2022 September 27; revised 2022 October 20; accepted 2022 October 27; published 2022 December 13

Abstract

With Mapping Nearby Galaxies at APO integral field spectroscopy, we present a resolved analysis of star formation for 29 jellyfish galaxies in nearby clusters, identified from radio continuum imaging taken by the Low Frequency Array. Simulations predict enhanced star formation on the "leading half" (LH) of galaxies undergoing ram pressure stripping, and in this work we report observational evidence for this elevated star formation. The dividing line (through the galaxy center) that maximizes this star formation enhancement is systematically tied to the observed direction of the ram-pressure-stripped tail, suggesting a physical connection between ram pressure and this star formation enhancement. We also present a case study on the distribution of molecular gas in one jellyfish galaxy from our sample, IC3949, using Atacama Large Millimeter/submillimeter Array CO $J = 1 - 0$, HCN $J = 1 - 0$, and HCO^+ $J = 1 - 0$ observations from the ALMA MaNGA Quenching and Star Formation Survey. The H_2 depletion time (as traced by CO) in IC3949 ranges from ∼1 Gyr in the outskirts of the molecular gas disk to ∼11 Gyr near the galaxy center. IC3949 shows a clear region of enhanced star formation on the LH of the galaxy where the average depletion time is ∼2.7 Gyr, in line with the median value for the galaxy on the whole. Dense gas tracers, HCN and HCO^+, are only detected at the galaxy center and on the LH of IC3949. Our results favor a scenario in which ram pressure compresses the interstellar medium, promoting the formation of molecular gas that in turn fuels a localized increase of star formation.

Unified Astronomy Thesaurus concepts: Galaxy clusters (584); Star formation (1569); Ram pressure stripped tails (2126); Galaxy quenching (2040); Molecular gas (1073)

Supporting material: figure set

1. Introduction

Galaxies in clusters are subject to a host of physical processes not experienced by galaxies isolated in the field. As galaxies infall toward the minimum of the cluster potential they are perturbed through gravitational interactions with other galaxies as well as hydrodynamical interactions with the dense intracluster medium (ICM). The perturbations can affect both the stellar distribution within galaxies as well as gas in the interstellar medium (ISM). This is seen through observations at low redshift, showing that the ratio between the number of quiescent and star-forming (or roughly speaking, red and blue) galaxies is strongly enhanced in galaxy clusters compared to galaxies in lower density environments or the field (e.g., Dressler 1980; Postman & Geller 1984; Croton et al. 2005; Peng et al. 2010; Wetzel et al. 2012; Lin et al. 2014; Brown et al. 2017; Jian et al. 2018; Davies et al. 2019). This is interpreted as evidence for expedited quenching of star formation in dense environments, likely a result of the cluster-specific processes that are outlined below.

Gravitational interactions include tidal effects that can remove both gas and stars from galaxies (e.g., Mayer et al. 2006; Chung et al. 2007) as well as repeated impulsive interactions between galaxies ("harassment"; e.g., Moore et al. 1996). Excluding the central brightest cluster galaxy, mergers are less common in galaxy clusters than lower density environments (i.e., groups) due to the high relative velocities between cluster galaxies, but still occur at a reduced rate (e.g., Jian et al. 2012). Hydrodynamical interactions with the hot ICM can both prevent the accretion of fresh gas onto galaxies ("starvation"; e.g., Larson et al. 1980; Peng et al. 2015) and directly remove warm/cold gas from galactic disks through ram pressure stripping (RPS; e.g., Gunn & Gott 1972; Quilis et al. 2000). In practice the prevention of gas accretion via starvation is likely driven by a modest ram pressure that is able to remove the weakly bound circumgalactic medium from galaxies; thus, while RPS and starvation are often treated as separate processes, they are in all likelihood closely connected to one another. Viscous stripping and thermal evaporation of cold gas also likely play some role in gas removal from cluster galaxies (e.g., Cowie & Songaila 1977; Nulsen 1982). While it is difficult to reliably disentangle the effects of these various hydrodynamical mechanisms observationally, it is clear that they have important implications for the future of gas content and star formation in cluster galaxies (Boselli et al. 2022; Cortese et al. 2021, and references therein).

While the importance of different quenching mechanisms is still a matter of debate, some consensus has emerged that RPS plays a significant role (e.g., Gavazzi et al. 2001;

Yagi et al. 2010; Poggianti et al. 2017; Boselli et al. 2018; Jaffé et al. 2018; Maier et al. 2019; Roberts et al. 2019; Ciocan et al. 2020; Boselli et al. 2022; Cortese et al. 2021). This is in part due to the identification of so-called "jellyfish galaxies" in nearby groups and clusters, which has allowed RPS to be studied more directly. These are star-forming galaxies observed to have one-sided tails extending beyond the galaxy disk that are believed to be the product of RPS. These tails have been observed across the electromagnetic spectrum, including ionized gas traced by X-rays (e.g., Sun et al. 2006, 2010; Poggianti et al. 2019; Sun et al. 2021), the UV continuum (e.g., Smith et al. 2010; Boissier et al. 2012; George et al. 2018; Mahajan et al. 2022), and Hα emission (e.g., Gavazzi et al. 2001; Yagi et al. 2010; Poggianti et al. 2017; Boselli et al. 2018); atomic gas traced by hydrogen 21 cm emission (e.g., Kenney et al. 2004; Oosterloo & van Gorkom 2005; Chung et al. 2009; Kenney et al. 2015; Hess et al. 2022); molecular gas traced by rotational transitions of the carbon monoxide molecule (Jáchym et al. 2017; Lee & Chung 2018; Jáchym et al. 2019; Moretti et al. 2020a, 2020b); and cosmic ray electrons traced by synchrotron emission in the radio continuum (e.g., Gavazzi & Jaffe 1987; Murphy et al. 2009; Chen et al. 2020; Roberts et al. 2021b). The strength of RPS scales with $\sim\rho v^2$, where ρ is the density of the ICM and v is the relative velocity between the galaxy and the ICM. Given the the dependence on ICM density and velocity dispersion, galaxies should experience stronger ram pressure in high-mass clusters compared to low-mass groups, a trend which is consistent with results from both simulations and observations (e.g., Yun et al. 2019; Roberts et al. 2021a, 2022b) and is also consistent with the fact that galaxy-quenched fractions in groups and clusters monotonically increase with host halo mass (e.g., Kimm et al. 2009; Wetzel et al. 2012). If the strength of the ram pressure exceeds the restoring gravitational potential of the galaxy then gas stripping can occur, which, if efficient, will remove a galaxy's reservoir of cold gas and thus quench star formation. If RPS is able to directly strip molecular gas then this quenching will occur very rapidly ($<$1 Gyr); however, if only atomic gas is efficiently removed then the quenching timescale will be longer and set by the depletion time of the remaining molecular gas reserve.

There is increasing evidence that RPS does not cause a simple, monotonic decrease in the star formation rate (SFR), and instead ram pressure can temporarily enhance star formation in galaxies (e.g., Gavazzi et al. 2001; Vulcani et al. 2018; Roberts & Parker 2020; Vulcani et al. 2020; Boselli et al. 2021; Cramer et al. 2021; Durret et al. 2021). This is likely a result of ISM compression induced by ram pressure that leads to high gas densities, efficient formation of molecular gas, and strong star formation (e.g., Schulz & Struck 2001; Moretti et al. 2020a, 2020b; Cramer et al. 2021). Theoretically this SFR enhancement should be strongest on the "leading half" (LH) of the galaxy where the ISM will be highly compressed by ram pressure (i.e., opposite to the direction of the stripped tail). From EAGLE simulations (Schaye et al. 2015), there is evidence that star formation is systematically enhanced by a factor of $\sim$1.1 to $\sim$1.5 on the LH of simulated galaxies in groups and clusters (Troncoso-Iribarren et al. 2020). Troncoso-Iribarren et al. (2020) use the direction of the three-dimensional velocity vector in order to split each galaxy into a LH and trailing half (TH). It is more difficult to directly test this prediction observationally as full velocity information is not observable and projection effects are unavoidable, but there are isolated examples of observed galaxies with asymmetric star formation that is thought to be induced by ram pressure on the LH (e.g., Gavazzi et al. 2001; Lee & Jang 2016; Boselli et al. 2021; Roberts et al. 2022a; Hess et al. 2022).

In this work we observationally address the question of whether or not star formation is enhanced on the LH of galaxies undergoing RPS. We use a sample of 29 jellyfish galaxies (Roberts et al. 2021b) identified on the basis of 144 MHz radio continuum tails observed by the LOw Frequency ARray (LOFAR; van Haarlem et al. 2013) that also have public integral field spectroscopy (IFS) from the Mapping Nearby Galaxies at APO (MaNGA; Bundy et al. 2015; Abdurro'uf et al. 2022) survey. Based on the observed tail directions relative to their host cluster centers (Roberts et al. 2021b), as well as the rarity of close galaxy neighbors for this sample of jellyfish galaxies, we believe that these tails are primarily produced via RPS, though we cannot fully rule out that tidal effects may contribute to some of the radio continuum asymmetries. This low-frequency continuum flux is tracing synchrotron emission from cosmic ray electrons moving through magnetic fields that extend from the stellar disk along the stripped tail. The LOFAR observations of these stripped tails are critical for this analysis as they allow us to estimate the direction of motion across the plane of the sky (i.e., opposite to the direction of the LOFAR radio continuum tail, modulo projection), thus defining the LH and TH of each galaxy. The MaNGA observations are equally important as they allow us to resolve the spatial distribution of star formation across these galaxies with extinction-corrected Hα maps. This unique data set is ideal for observationally testing the prediction of enhanced star formation on the LH of jellyfish galaxies. Furthermore, this work introduces a sample of LOFAR-MaNGA jellyfish galaxies that can be utilized, moving forward, to study the resolved properties across the disks of galaxies undergoing RPS in nearby clusters. Finally, we present a case study of the connection between star formation and molecular gas in the jellyfish galaxy IC3949, including a region of ram-pressure-induced star formation. This analysis adds to the rapidly growing number of studies focused on the molecular gas content of galaxies undergoing RPS (e.g., Vollmer et al. 2012; Jáchym et al. 2014, 2017; Lee et al. 2017; Jáchym et al. 2019; Moretti et al. 2020a, 2020b; Cramer et al. 2020, 2021; Lee et al. 2022a; Cramer et al. 2022; Zabel et al. 2022), and, to the best of our knowledge, this is the first analysis of dense molecular gas tracers (HCN and HCO^+) in a jellyfish galaxy.

The outline of this paper is as follows. In Section 2 we describe the galaxy samples used in this work along with the derived data products. In Section 3 we present evidence for enhanced star formation on the LH of jellyfish galaxies. In Section 4 we present a case study on the connection between star formation and molecular gas in the jellyfish galaxy IC3949. Finally, in Section 5 we provide a brief discussion of the main results of this work and give concluding statements. Throughout this manuscript we assume a flat Lambda cold dark matter cosmology with (Ω_M, Ω_Λ, H_0) = (0.3, 0.7, 70 km s^{-1} Mpc^{-1}) and a Salpeter initial mass function (Salpeter 1955).

2. Data

In this work we use public IFS from the MaNGA survey to explore the spatial distribution of star formation in both jellyfish galaxies in nearby clusters and a matched control sample of

noncluster galaxies. Below we describe the selection of these two galaxy samples. For both the control and jellyfish samples we use integrated galaxy stellar masses from the Pipe3D catalog (Sánchez et al. 2016a, 2016b) and redshifts from Sloan Digital Sky Survey (SDSS) spectroscopy.

2.1. Jellyfish Galaxy Sample

Our parent sample of jellyfish galaxies is taken from Roberts et al. (2021b). From a large sample of star-forming galaxies in low-redshift clusters ($z < 0.05$), Roberts et al. (2021b) identify 95 jellyfish galaxies on the basis of one-sided radio continuum tails observed by LOFAR at 144 MHz as part of the LOFAR Two Meter Sky Survey (LoTSS; Shimwell et al. 2022). We match these 95 jellyfish galaxies against the final data release from the MaNGA survey (SDSS Data Release 17, DR17; Abdurro'uf et al. 2022) that includes public IFS for ∼10,000 galaxies in the main galaxy sample. Of the 95 jellyfish galaxies from Roberts et al. (2021b), 30 have MaNGA IFS. Sixteen of these 30 galaxies are part of the Coma Cluster, 10/30 are part of the A2197/A2199 system, 2/30 are part of the NGC6338 group, 1/30 is part of the NGC5098 group, and 1/30 is part of A2593. In Figure 1 (left-hand column) we show optical plus LOFAR overlay images for the galaxies that make up our final jellyfish galaxy sample.

For these 30 galaxies we isolate star-forming spaxels according to emission line diagnostic diagrams (Baldwin et al. 1981). We first mask all spaxels with signal-to-noise ratio (S/N) < 3 in Hα, Hβ, [OIII], [NII], or [SII]; we then mask all spaxels with EW(Hα) < 3 Å; and, finally, mask any spaxels that are not classified as "star-forming" according to both the [OIII]/Hβ versus [NII]/Hα and [OIII]/Hβ versus [SII]/Hα dividing lines from Kewley et al. (2001, 2006). We note that this does not exclude spaxels that would be classified as "composite" between the Kewley et al. (2001) and Kauffmann et al. (2003) dividing lines on the [OIII]/Hβ versus [NII]/Hα diagram. We reran our analysis with a stricter selection for star-forming spaxels where we only included spaxels that had EW(Hα) > 6 Å and added a requirement that spaxels are classified as "star-forming" according to the Kauffmann et al. (2003) dividing line on the [OIII]/Hβ versus [NII]/Hα diagram. This did not qualitatively change any of the conclusions from this work: therefore we opt for the slightly looser criteria which includes composite spaxels to avoid overmasking weakly star-forming regions. This star-forming spaxel selection results in one galaxy being completely removed from our sample (MaNGA plate-ifu: 11943-6104) as all of the detected spaxels for this galaxy are classified as Seyfert active galactic nucleus (AGN); however, the remaining 29 galaxies show emission dominated by star formation with a minority of spaxels masked due to this selection. With non-star-forming spaxels masked we produce resolved SFR surface density maps, $\Sigma_{\rm SFR}$, for each jellyfish galaxy based on the MaNGA Hα emission line maps. We correct the Hα line fluxes for dust extinction using the Balmer decrement determined for each spaxel (see the Appendix of Vogt et al. 2013 for a detailed description). The SFR for each spaxel is calculated from the dust-corrected Hα luminosity using the calibration from Kennicutt (1998a). We then convert the SFR to a surface density in $M_\odot\,{\rm yr}^{-1}\,{\rm kpc}^{-2}$ using the MaNGA spaxel dimensions of $0\farcs5 \times 0\farcs5$ and the luminosity distance to the host cluster. We obtain resolved stellar mass maps from the Pipe3D Value Added Catalogs (Sánchez et al. 2016a, 2016b; Lacerda et al. 2022). We use the stellar mass maps with dust corrections and apply the "dezonification" map to each stellar mass map in order to reduce the signature of the Voronoi binning (see Cid Fernandes et al. 2013 for details). After multiplying by the dezonification map we follow Sánchez et al. (2016b) and smooth each stellar mass map with a Gaussian kernel with a FWHM equal to the MaNGA r-band FWHM (∼2″–3″, depending on the galaxy). Again, we convert the stellar mass maps to surface densities, $\Sigma_\star$, with units of $M_\odot\,{\rm kpc}^{-2}$. All spaxels with S/N < 3 as well as all spaxels with $\Sigma_\star < 10^7\,M_\odot\,{\rm kpc}^{-2}$ in the stellar mass maps are masked. Both SFR and stellar mass surface density maps are inclination corrected using the optical axis ratio (b/a) for each galaxy taken from the NASA-Sloan Atlas. Finally, we create resolved maps of specific star formation rate (sSFR = SFR/$M_\star$) by taking the ratio of the SFR and stellar mass surface density maps. In Figure 1 (right-hand three columns) we show the SFR surface density, stellar mass surface density, and sSFR maps for each jellyfish galaxy.

2.2. Control Galaxy Sample

We also compile a sample of matched control galaxies that are not members of massive groups or galaxy clusters. Comparing our results for jellyfish galaxies to the same properties measured for our control sample is critical for isolating the influence of the cluster environment, and in turn the process of RPS. We note that even galaxies in that are not in massive groups or clusters (e.g., galaxy pairs) can experience "environmental-like" effects on their star formation (e.g., Moon et al. 2019; Yang et al. 2022). It is possible that cases such as this exist in our control sample, but the implicit assumption that we are making is that these types of perturbations will be significantly smaller than those experienced by satellite galaxies in massive clusters. To generate our matched control sample we first consider all star-forming galaxies (i.e., sSFR > $10^{-11}\,{\rm yr}^{-1}$) in the Data Release 17 (DR17) MaNGA release (Abdurro'uf et al. 2022). We then restrict this to only those galaxies that are isolated (i.e., part of a single-member "group") or part of a group with halo mass, M_H, $<10^{13}\,M_\odot$ in the Lim et al. (2017) SDSS group/cluster catalog. This ensures that our control sample does not contain galaxies in clusters or massive groups. We also restrict this sample to only contain galaxies that are detected by LOFAR at 144 MHz as part of the LoTSS Data Release 2 source catalog (Williams et al. 2019; Shimwell et al. 2022). This matches the selection criteria for the LOFAR jellyfish galaxy sample, which by definition are detected at 144 MHz.

At this point we have an "unmatched" control sample of ∼800 star-forming MaNGA galaxies in low-density environments that have significant radio continuum emission at 144 MHz. We now match this sample to the stellar mass and redshift distribution of the jellyfish galaxy sample. By matching in stellar mass and redshift we ensure that the comparison between the jellyfish and control samples is unbiased in terms of differences in galaxy mass and physical resolution. For each jellyfish galaxy we find all galaxies in the unmatched control sample where:

1. the control galaxy and jellyfish galaxy stellar masses are consistent within their respective 1σ error ranges; and
2. the difference between the control galaxy and jellyfish galaxy redshifts is given by $\Delta z < 0.005$.

This gives a list of matches for each jellyfish galaxy, some jellyfish galaxies having ∼5 matched galaxies and some having

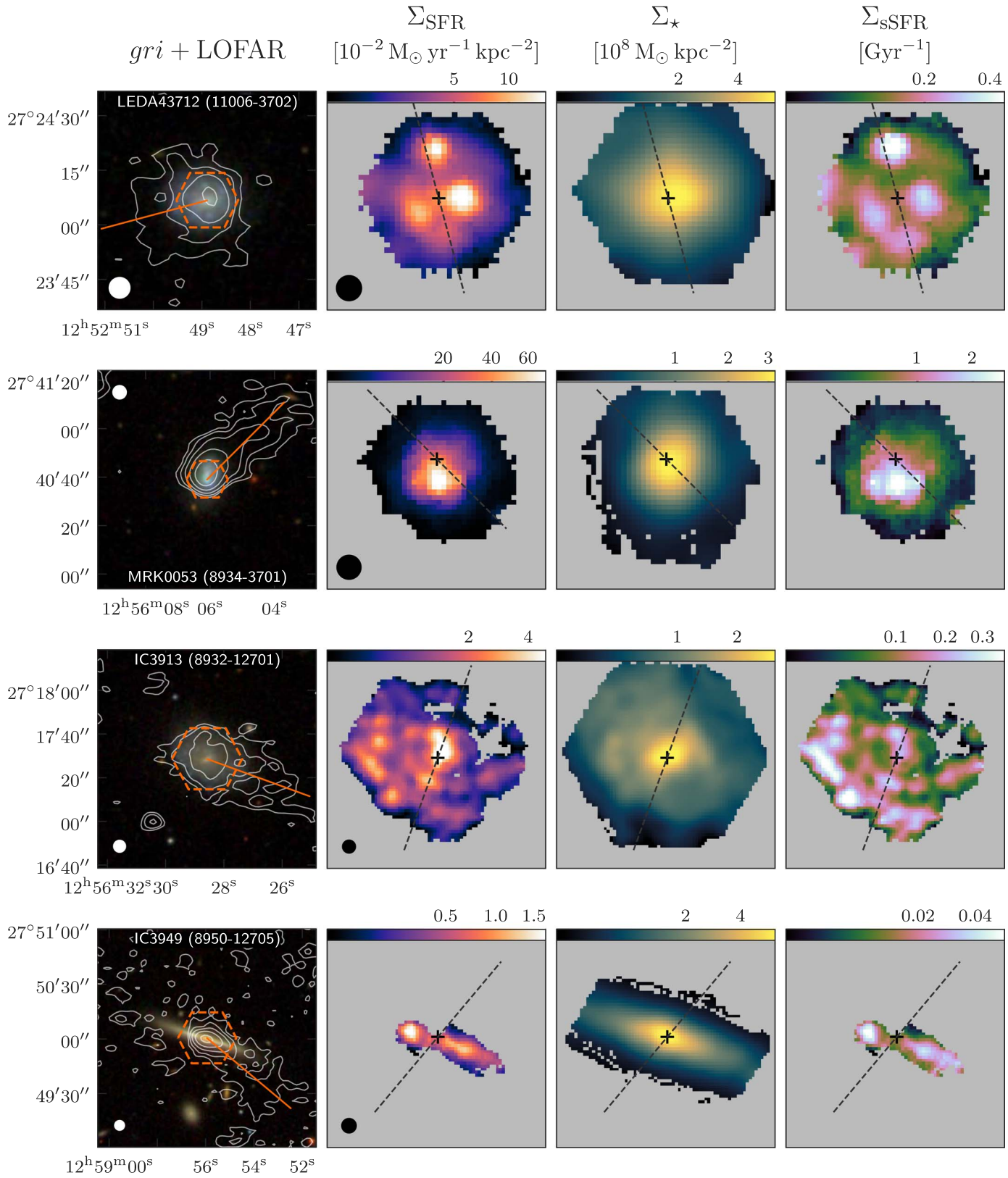

Figure 1. Left to right: SDSS optical image plus LOFAR contours at the (2, 4, 8, 16, ...) σ levels, star formation rate surface density map, stellar mass surface density map, and specific star formation rate surface density map. The white circle shows the 6″ LOFAR beam, the orange hexagon and line show the MaNGA field of view and the tail orientation, the black circle shows the MaNGA FWHM r-band resolution, and the black dashed line divides the leading and trailing halves. The complete figure set (8 images) is available in the online journal.

(The complete figure set (8 images) is available.)

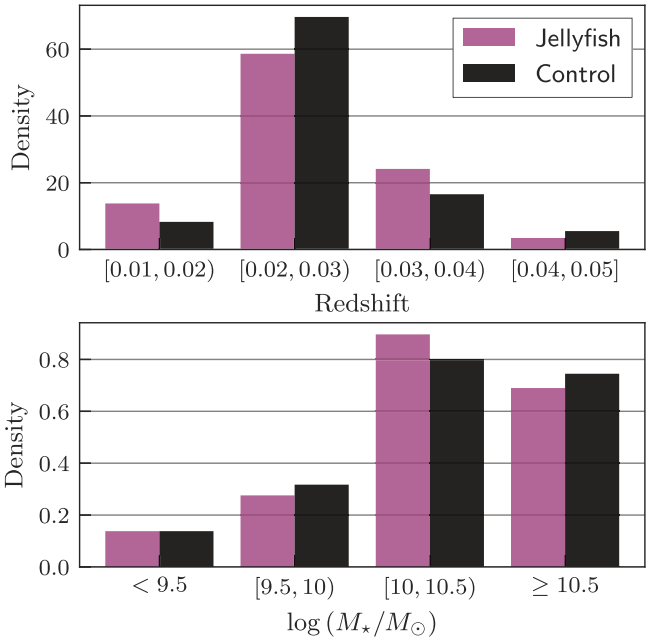

Figure 2. Redshift and integrated stellar mass distributions for jellyfish galaxies (magenta) and galaxies in the control sample (black).

tens of matched galaxies. To ensure that all jellyfish galaxies have equal weight in the final matched control sample, we randomly draw five matched control galaxies for each jellyfish galaxy, giving a final control sample of 145 galaxies that are well matched to the jellyfish galaxy sample. The redshift and stellar mass distributions for both the jellyfish and control galaxy samples are shown in Figure 2.

3. Enhanced Star Formation on the Leading Half

A primary question that we address in this work is whether or not star formation is enhanced on the LH of jellyfish galaxies (i.e., the galaxy side opposite to the direction of the RPS tail). Enhanced star formation on the LH of group and cluster galaxies in the EAGLE simulations was reported by Troncoso-Iribarren et al. (2020), which they argue is a result of gas compression in the ISM due to ram pressure. This work is an observational test of this prediction from hydrodynamical simulations.

3.1. Star Formation Anisotropy

In Troncoso-Iribarren et al. (2020) the "leading" and "trailing" halves of galaxies are defined relative to the three-dimensional velocity vector for each galaxy, such that the plane that passes through the galaxy center and is normal to the velocity vector divides the LH and TH. This is a natural choice as ram pressure is maximal along the direction of motion, but the three-dimensional velocity vector is not an observable quantity. We approximate this by using the direction of the observed radio continuum tail as a proxy for the direction of motion for each of the jellyfish galaxies in our sample. Tail directions are taken from Roberts et al. (2021b) and range between 0° and 360°, where 0° = west and 90° = north. We assume that the radio continuum tail points opposite to the direction of motion, and thus we observationally divide the LH and TH by the line passing through the optical galaxy center that is normal to the projected tail direction. For each galaxy in our control sample we also define a LH and TH by dividing the galaxy with a line through the optical galaxy center at a random orientation. This division is not physically motivated but it does quantify the level of intrinsic anisotropy expected between two halves of a "normal" galaxy not part of an overdense environment. This allows us to isolate the impact of environment for our jellyfish sample by determining whether anisotropies between the LH and TH of jellyfish galaxies systematically differ from those found by randomly dividing galaxies in our control sample.

With a LH and TH defined for each galaxy in our jellyfish and control samples, we now define two quantities, the sSFR excess and the SFR excess, to measure the degree of star formation anisotropy between these two galaxy halves. We calculate these quantities as follows:

$$\text{sSFR excess} = \log_{10}(\,\overline{\text{sSFR}}_{\text{LH}}/\overline{\text{sSFR}}_{\text{TH}}\,), \quad (1)$$

and

$$\text{SFR excess} = \log_{10}(\,\overline{\text{SFR}}_{\text{LH}}/\overline{\text{SFR}}_{\text{TH}}\,), \quad (2)$$

where $\overline{\text{sSFR}}_{\text{LH}}$ and $\overline{\text{sSFR}}_{\text{TH}}$ are the average sSFRs measured over the LH and TH of the galaxy, and $\overline{\text{SFR}}_{\text{LH}}$ and $\overline{\text{SFR}}_{\text{TH}}$ are defined analogously for SFR. Positive values of the sSFR and SFR excess indicate enhanced star formation on the LH relative to the TH and vice versa for sSFR/SFR excess < 0. We list the measured sSFR excess and SFR excess values for each jellyfish galaxy in Table 1. There are six jellyfish galaxies in our sample (MaNGA plate-ifus: 8931-3703, 8442-1901, 12673-6101,

Table 1
Jellyfish Galaxy sSFR and SFR Excess

Name	Plate-ifu	sSFR Excess	SFR Excess
LEDA43712	11006-3702	-0.09 ± 0.02	0.01 ± 0.02
MRK0053	8934-3701	0.3 ± 0.04	0.31 ± 0.04
IC3913	8932-12701	0.13 ± 0.01	0.16 ± 0.01
IC3949	8950-12705	0.06 ± 0.03	0.16 ± 0.03
IC0837	11009-12704	-0.07 ± 0.02	-0.18 ± 0.02
GMP4351	9876-3702	-0.06 ± 0.04	0.14 ± 0.04
MRK0056	11014-3704	0.2 ± 0.03	0.07 ± 0.03
MRK0057	8932-3701	0.12 ± 0.01	0.13 ± 0.01
GMP3509[a]	8931-3703	0.09 ± 0.02	0.05 ± 0.02
GMP3271	9876-3703	0.01 ± 0.03	0.19 ± 0.03
GMP2601	9863-12701	0.0 ± 0.02	0.04 ± 0.02
GMP2599	9862-9101	0.08 ± 0.02	0.24 ± 0.02
GMP1616	8935-6104	-0.18 ± 0.03	-0.15 ± 0.03
GMP1576	9876-6101	0.12 ± 0.02	0.12 ± 0.02
GMP0455	11004-12701	0.36 ± 0.02	0.38 ± 0.02
LEDA2017338[a]	8442-1901	-0.05 ± 0.04	0.16 ± 0.04
LEDA2168096[a]	12673-6101	0.19 ± 0.03	0.18 ± 0.03
LEDA2175783[a]	11942-6103	0.26 ± 0.04	0.11 ± 0.04
LEDA58067	8603-9102	0.07 ± 0.01	0.15 ± 0.01
MRK0881	8604-9102	-0.25 ± 0.02	-0.21 ± 0.02
LEDA2156782	8550-3701	-0.01 ± 0.04	0.01 ± 0.04
LEDA58296	8312-12703	0.06 ± 0.01	0.1 ± 0.01
LEDA2147644[a]	9869-12702	0.04 ± 0.02	0.3 ± 0.02
LEDA58307[a]	9869-9102	0.2 ± 0.03	0.07 ± 0.03
UGC10429	8550-6103	0.15 ± 0.02	0.06 ± 0.02
LEDA2568088	8625-9102	0.08 ± 0.01	-0.0 ± 0.01
LEDA2566358	8625-12702	0.24 ± 0.02	0.23 ± 0.02
LEDA1479719	8622-6103	-0.05 ± 0.02	0.09 ± 0.02

Note.
[a] Σ_{SFR} map is only marginally resolved along the axis of the radio tail.

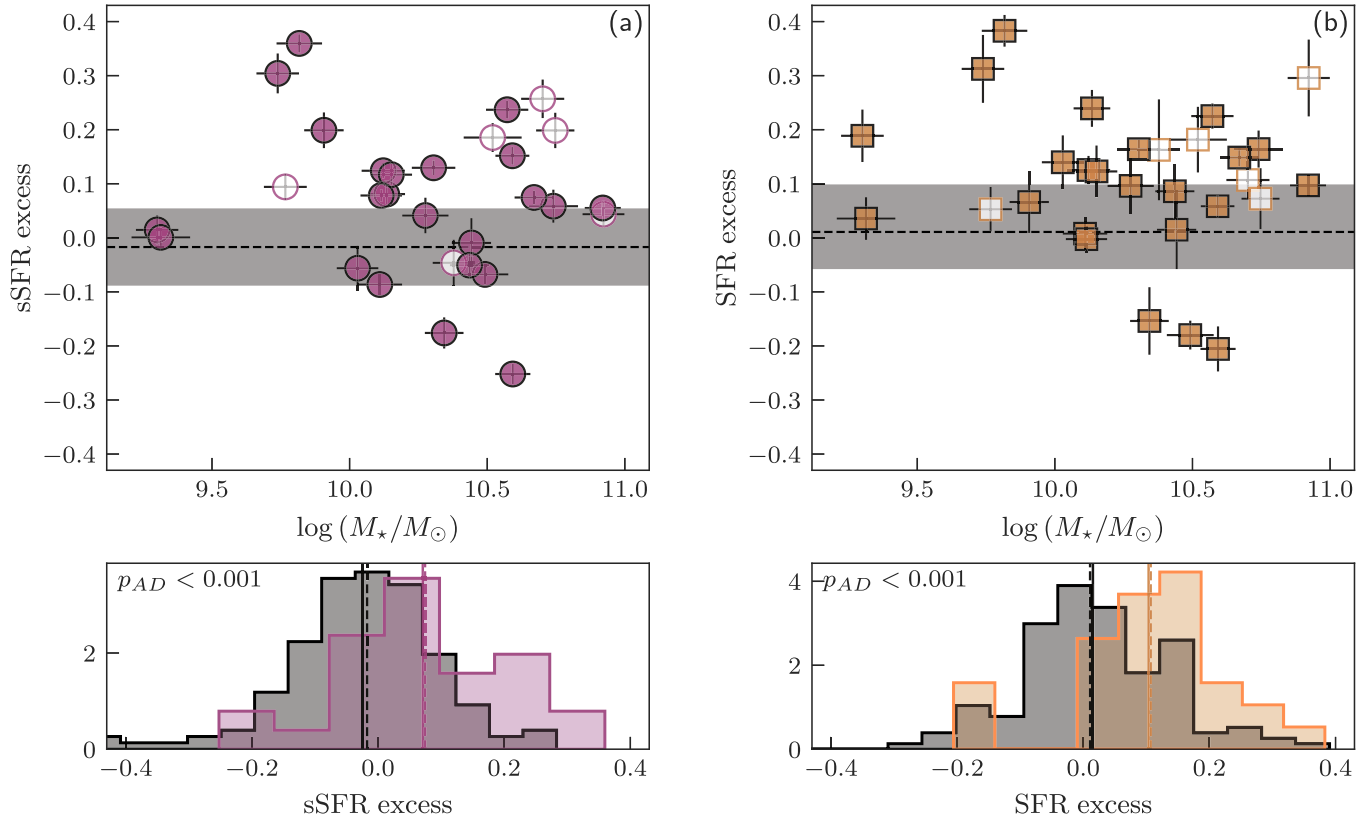

Figure 3. Left, top: sSFR excess (see text for details) vs. galaxy stellar mass. Data points correspond to the jellyfish galaxy sample, error bars on ΔsSFR are calculated from bootstrap resampling, and error bars on stellar masses are taken from the Pipe3D catalog. The open markers correspond to the six jellyfish galaxies with marginally resolved Σ_{SFR} maps (along the axis of the observed tail), since the sSFR/SFR excess measurements for these galaxies are less reliable than the rest of the sample. The dashed line shows the median ΔsSFR for the control sample and the shaded region encloses the interquartile range. Left, bottom: distributions of the sSFR excess for the jellyfish galaxy and control samples. Median (dashed) and mean (solid) are shown with the vertical lines. Right: same as left-hand panel but for the SFR excess (see text for details).

11942-103, 9869-12702, and 9869-9102) where only ∼2 resolution elements (MaNGA *r*-band FWHM) span across the Σ_{SFR} map along the axis of the observed radio tail. These are primarily edge-on galaxies with stripped tails that are roughly aligned with the galaxy minor axis. For these galaxies, the distinction between LH and TH is only marginally resolved, and thus the measurement of sSFR/SFR excess is likely less reliable than for the rest of the sample. We have tested removing these galaxies from the sample and rerunning our analysis, and we confirm that the qualitative results from this work do not change based on the inclusion or exclusion of these six galaxies. The median sSFR/SFR excess for the jellyfish sample is 0.07/0.11 when including these poorly resolved cases and 0.06/0.10 when excluding them. We opt to include these galaxies in our analysis but highlight them with open markers in Figures 3, 5, and 6, and with asterisks in Table 1.

In Figure 3(a) we show the sSFR excess and in Figure 3(b) we show the SFR excess, both plotted against integrated galaxy stellar mass for galaxies in our jellyfish sample. We also show the median sSFR and SFR excess for our control sample (dashed line) as well as the interquartile range (shaded regions). Jellyfish galaxies are skewed to positive values for both the sSFR and SFR excess; this is clear both in the upper panels of Figure 3 as well as lower panels, where we show the mean/median (solid/dashed vertical lines) values and the full distributions of sSFR and SFR excess for both the jellyfish and the control samples. For the control sample the sSFR and SFR excess is centered on zero, which is expected given that we are defining the LH and TH along a random axis for these galaxies. There is statistical evidence that the distributions of the sSFR excess and SFR excess for jellyfish galaxies and galaxies in the control sample are distinct. According to the two-sample Anderson–Darling test (Scholz & Stephens 1987), this difference is significant at >99.9% significance for both sSFR and SFR. While the distributions of sSFR and SFR excess for jellyfish galaxies are skewed to positive values and are consistent with enhanced star formation on the LH, not all jellyfish galaxies show this signature. A ram-pressure-induced burst of star formation is likely a transient phenomenon and thus we do not expect to observe all jellyfish galaxies in this state. It is also possible that for some galaxies there is a clear star formation excess signal in three dimensions that is being obscured by projection effects. Furthermore, the degree to which the ISM is perturbed by ram pressure will depend on a given galaxy's orbital history and position within its host cluster. We explore whether jellyfish galaxies with enhanced star formation on the LH occupy a distinct part of projected phase space relative to jellyfish galaxies without strong SFR anisotropies, but do not find any significant difference. If we divide our sample into two subsamples split at the median value of the SFR excess (the results are similar for sSFR excess) then the median and interquartile range of the clustercentric radius (i.e., R/R_{180} as given in Roberts et al. 2021b) distribution is 0.41 [0.22, 0.53] for galaxies with large excesses and 0.37 [0.28, 0.48] for galaxies with small excesses. Doing the same for the velocity

offset (i.e., $c\Delta z/\sigma$ as given in Roberts et al. 2021b) gives 0.69 [0.45, 1.95] for galaxies with large excesses and 0.75 [0.40, 1.55] for galaxies with small excesses. According to the two-sample Anderson–Darling test there is no evidence for a difference between the phase-space distributions for galaxies with large and small star formation excesses, but we note that with our modest sample size of 29 jellyfish galaxies it is difficult to subdivide the sample in such a way while maintaining statistical power.

Troncoso-Iribarren et al. (2020) compute an analogous quantity to our SFR excess for the simulated group/cluster galaxies in their work (Equation (8) in Troncoso-Iribarren et al. 2020). In these simulations the SFR for each gas particle is set according to the observed Kennicutt–Schmidt (KS) relation, with a metallicity-dependent density threshold to prevent the unrealistic case of hot, low-density gas-forming stars. We note that these SFR excesses are measured in a relative sense within individual galaxies, and this adds some degree of robustness in terms of uncertainties surrounding the specifics of star formation prescriptions between observations and simulations. In their simulated data, Troncoso-Iribarren et al. (2020) find enhanced star formation on the LH with a typical SFR excess of $\sim$0.05. They show that their simulated group/cluster galaxies have enhanced gas pressures on their leading sides (both relative to the trailing sides and relative to EAGLE main-sequence galaxies). This increased pressure feeds into their SFR prescription (Equation (1) in Troncoso-Iribarren et al. 2020) and thus this SFR excess is attributed to this gas compression on the leading side. We find a typical SFR excess of $\sim$0.1 for the observed jellyfish galaxies in this work, slightly larger than is found by Troncoso-Iribarren et al. (2020). This contrast may be explained by differences in the sample definitions. In particular, Troncoso-Iribarren et al. (2020) include all star-forming group/cluster galaxies from the simulation box in their analysis, whereas we are restricted to only star-forming galaxies with an observed radio continuum tail. Our jellyfish galaxy sample is likely skewed toward stronger RPS in order to produce an observable tail, which in turn may drive a stronger enhancement of star formation on the LH. Furthermore, our jellyfish sample is drawn from massive clusters ($M_{\rm halo} > 10^{14} M_{\odot}$), whereas the galaxy sample in Troncoso-Iribarren et al. (2020) has a substantial number of galaxies hosted by group-mass systems ($M_{\rm halo} < 10^{14} M_{\odot}$). Roberts et al. (2021a) and Roberts et al. (2022b) have shown that global SFR enhancements in galaxies undergoing RPS are stronger in massive clusters and more marginal in group-mass systems. All said, the qualitative results between this work and Troncoso-Iribarren et al. (2020) are in good agreement, as both works find evidence for enhanced star formation on the LH of galaxies likely due to RPS.

3.2. Maximizing the Star Formation Anisotropy

In the previous section we show that our sample of jellyfish galaxies display evidence for enhanced star formation on their LH, opposite to the direction of the RPS tail. We define the LH and TH of our galaxies according to the direction of observed radio continuum tails, though an alternative approach to quantify star formation anisotropy in galaxies is with a dividing line that maximizes the sSFR or SFR excess. In the case of ram-pressure-induced star formation from gas compression, these two definitions should be similar. In other words, if ram pressure is driving enhanced star formation, then the dividing line that maximizes the sSFR or SFR excess should be roughly normal to the observed tail direction (modulo projection effects). Maximizing this star formation anisotropy is also suggested by Troncoso-Iribarren et al. (2020) as a viable method for determining the LH and TH of group/cluster galaxies observationally, which may be particularly useful in cases where a clear RPS tail is not observed.

In this section we test how closely our definition of the LH and TH (based on the observed tail directions) corresponds to the dividing line that maximizes the sSFR and SFR excess for each galaxy. For each jellyfish galaxy we first find two maximal dividing lines: one to maximize the sSFR excess and one to maximize the SFR excess. All dividing lines must pass through the optical galaxy center and are otherwise defined by an orientation, α, where $\alpha \in [0^{\circ}, 360^{\circ})$. An orientation of 0° corresponds to a horizontal line along the W–E axis with the northern side of the galaxy as the LH, and an orientation of 90° corresponds to a vertical line along the N–S axis with the eastern side of the galaxy as the LH. From the orientation that maximizes the sSFR and SFR excess, $\alpha_{\rm max,\ sSFR}$ and $\alpha_{\rm max,\ SFR}$, we then infer a "tail direction" that is normal to this angle and can be compared to the observed tail direction. In Figure 4 we show these different tail direction definitions graphically, and in Figure 5 we plot the sSFR/SFR excess versus the difference between the observed tail direction and the direction that is normal to the line maximizing the sSFR excess ($\Delta\theta_{\rm sSFR}$) and the SFR excess ($\Delta\theta_{\rm SFR}$). A value of 0° corresponds to the case where the tail direction inferred from maximizing the sSFR/SFR excess is identical to the observed tail direction, for 90° the two are perpendicular, and for 180° the two point in opposite directions. In Figure 5 there is a clear anticorrelation between both the sSFR excess and $\Delta\theta_{\rm sSFR}$ as well as the SFR excess and $\Delta\theta_{\rm SFR}$. This shows that jellyfish galaxies with large sSFR/SFR excess also have observed tail directions that roughly maximize the difference in star formation between the LH and TH, in agreement with expectations from RPS. Jellyfish galaxies with sSFR/SFR excess ~ 0 have values of $\Delta\theta_{\rm sSFR}$ and $\Delta\theta_{\rm SFR}$ that span the full range between 0° and 180° and thus do no appear to be tied to the observed tail direction. Finally, there is a hint that the few galaxies with large negative sSFR/SFR excesses tend to have $\Delta\theta_{\rm sSFR/SFR}$ near 180°. Even in these cases the orientation that maximizes the sSFR/SFR excess seems to be connected to the tail direction. This may be an indicator of star formation occurring in the stripped gas being transported along the tail direction; we also briefly discuss this possibility in the next Section 3.3. If strong star formation anistropies are observed in cluster galaxies, these results suggest that it may be possible to infer a RPS tail direction by maximizing this anisotropy (as also suggested by Troncoso-Iribarren et al. 2020). That said, such an exercise should always be taken with significant caution as there are physical mechanisms in cluster environments beyond RPS that can produce asymmetric star formation.

3.3. Locating the Peak of (Specific) Star Formation

In Sections 3.1 and 3.2 we have shown that jellyfish galaxies have enhanced sSFRs on their LH and that the dividing line between the LH and TH inferred from observed tail directions is close to the dividing line that maximizes the star formation anisotropy for the majority of jellyfish galaxies in our sample. As a final test to confirm enhanced star formation on the LH of these galaxies we explore the position of the sSFR peak for

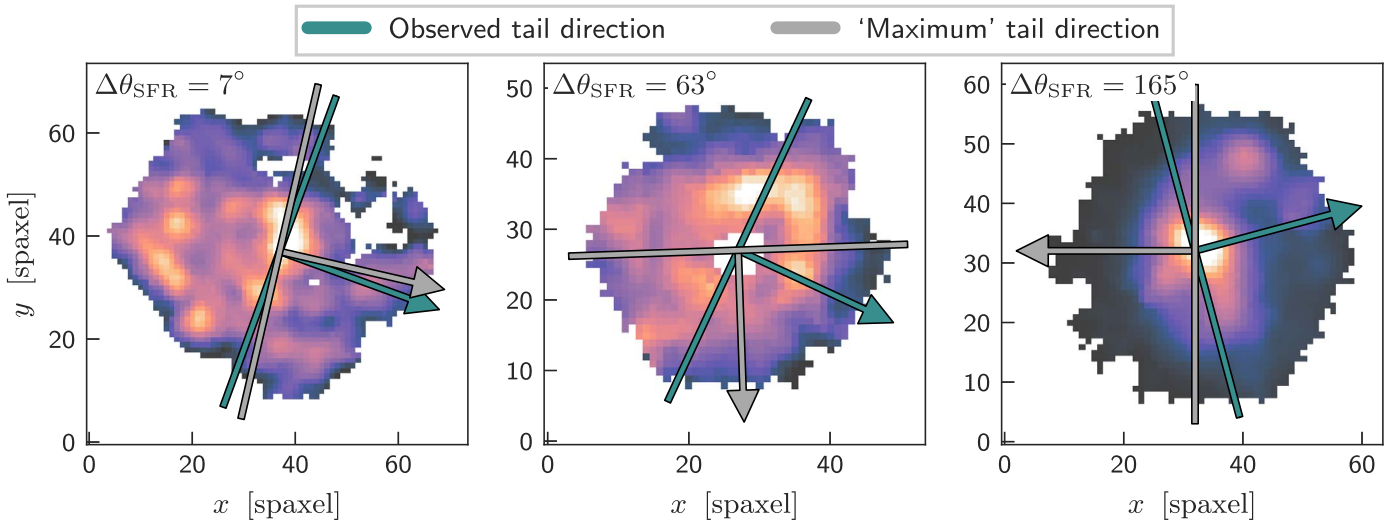

Figure 4. Example schematics showing the observed tail direction (teal arrow) and the "tail direction" that is inferred by maximizing the SFR excess (gray arrow), overlaid on the SFR surface density maps. The solid lines show the corresponding divisions between the leading and trailing sides. We show three examples, one with $\Delta\theta_{\rm SFR} \sim 0$ (IC3913), one with an intermediate value of $\Delta\theta_{\rm SFR}$ (UGC10429), and one with $\Delta\theta_{\rm SFR} \sim 180$ (MRK0881).

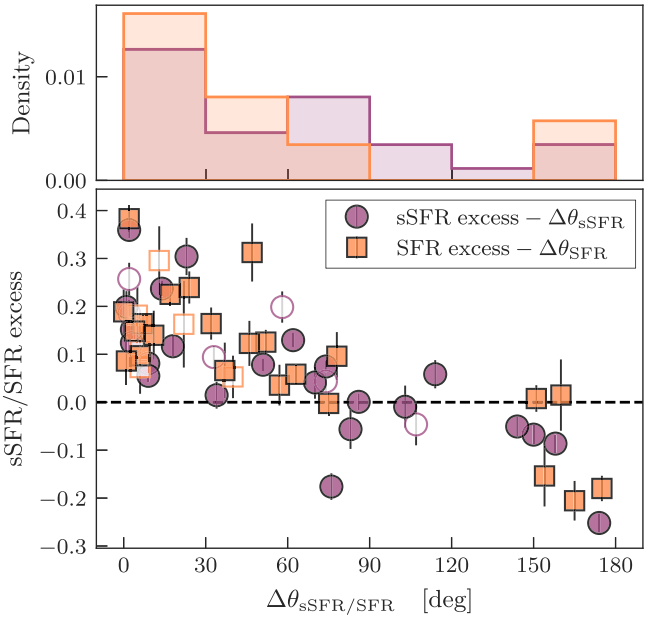

Figure 5. sSFR/SFR excess vs. the offset between the axis which maximizes the star formation anisotropy and the LH–TH axis inferred from the observed tail direction. Star formation anisotropies measured with the sSFR excess are shown with magenta circles and star formation anisotropies measured with the SFR excess are shown with orange squares. Error bars on the sSFR/SFR excess are calculated from bootstrap resampling. The open markers correspond to the six jellyfish galaxies with marginally resolved $\Sigma_{\rm SFR}$ maps (along the axis of the observed tail). In the upper panel we also show histograms of the distribution of $\Delta\theta_{\rm sSFR}$ and $\Delta\theta_{\rm SFR}$.

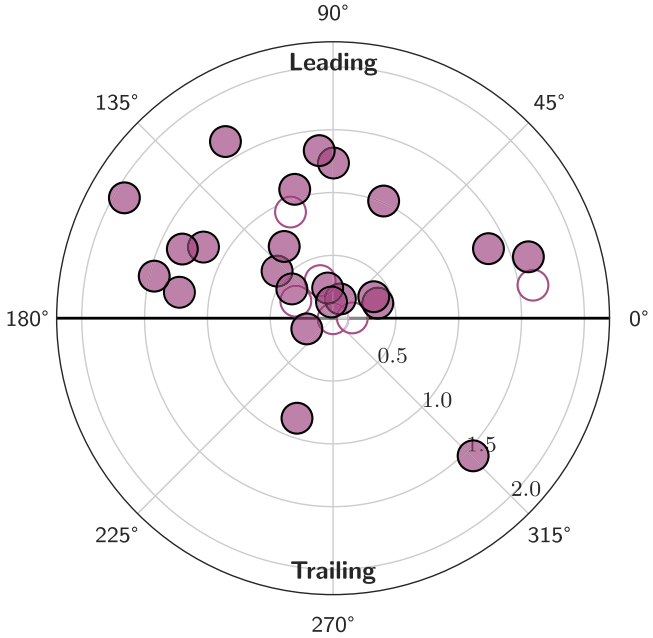

Figure 6. The location of the specific star formation rate peak for each jellyfish galaxy in polar coordinates. The azimuthal axis shows the orientation between the sSFR peak and the observed tail (see text for details) and the radial axis shows the radial offset of the sSFR peak from the galaxy center in units of the galaxy effective radius. The open markers correspond to the six jellyfish galaxies with marginally resolved $\Sigma_{\rm SFR}$ maps (along the axis of the observed tail).

each galaxy with respect to the observed radio continuum tail. We use the peak of sSFR instead of SFR since most galaxies will have a SFR peak near the galaxy center due to the high concentration of mass, whereas by using sSFR we are probing a relative increase in SFR modulated by the local stellar mass surface density.

We identify the position of the pixel with the highest sSFR, $p_{\rm max} = (x_{\rm max}, y_{\rm max})$, and compare the location of $p_{\rm max}$ to the observed direction of the stripped tail. When determining $p_{\rm max}$ we filter the sSFR map with a 3×3 uniform kernel such that each pixel is averaged with its eight nearest neighbors. This is to ensure that our measurement is robust against random pixel-to-pixel varations. We quantify the orientation between the two with an angle such that $p_{\rm max}$ on the LH of the galaxy will have an orientation between 0° and 180° (with 90° is directly opposite to the tail direction) and $p_{\rm max}$ on the TH will have an orientation between 180° and 360° (with 270° being directly in line with the tail). For brevity we will refer to this orientation as $\Delta\varphi$. We also record the radial offset of $p_{\rm max}$ with respect to the galaxy center in units of the galaxy effective radius, which we denote as $r_{\rm max}$. In Figure 6 we plot $\Delta\varphi$ (azimuthal axis) and $r_{\rm max}$ (radial axis) on a polar plot for each jellyfish galaxy. The distribution of points is asymmetric, with the majority of

jellyfish galaxies having $0 < \Delta\varphi < 180$, demonstrating that the regions of peak star formation (per unit stellar mass) are systematically found on the LH. The two galaxies in Figure 6 with sSFR peaks that are on the TH and significantly offset from the galaxy center are GMP2599 (MaNGA plate-ifu: 9862-9101) and MRK0881 (MaNGA plate-ifu: 8604-9102). These sSFR peaks may be indicative of ongoing star formation along the stripped tail for these galaxies, as has been seen previously for some jellyfish galaxies (e.g., Gavazzi et al. 2001; Yagi et al. 2010; Poggianti et al. 2017; Boselli et al. 2018; Lee et al. 2022b; Hess et al. 2022). The MaNGA field of view (FOV) is too small to directly probe these stripped tails; however, for both galaxies the Hα emission fills the MaNGA FOV toward the direction of the observed radio tail, suggesting that there may be extraplanar star formation along the tail beyond the MaNGA coverage.

4. A Molecular Gas Case Study: IC3949

IC3949 (MaNGA plate-ifu: 8950-12705) is a massive ($\log[M_\star/M_\odot] \simeq 10.7$), edge-on disk galaxy located at the center of the Coma Cluster ($R/R_{180} = 0.1$; Roberts et al. 2021b) that is undergoing RPS. IC3949 shows a stripped tail to the SW that was first identified by Yagi et al. (2010) through narrow-band Hα observations. This tail has since been confirmed in the radio continuum at both 144 MHz (Roberts et al. 2021b) and 350 MHz (Lal et al. 2022). IC3949 is seemingly at an advanced quenching stage as it shows a highly truncated Hα disk (relative to the optical extent of the galaxy) and a low integrated SFR for its stellar mass (SFR $\approx 0.7\,M_\odot\,\mathrm{yr}^{-1}$; Salim et al. 2016, 2018) that places it in the so-called "green valley." In Figure 7(a) we show a near-UV image (F350LP) of IC3949 taken by the Hubble Space Telescope. This image shows UV continuum emission from the star-forming disk along with a complex dust morphology visible through extinction. Filaments of dust are visible extending to the S/SW in the direction of the observed radio continuum tail, likely being stripped by ram pressure. The most prominent region of dust extinction is cospatial with the region of enhanced star formation on the leading side of the disk (see Figure 1 and the open circle in Figure 7(a)).

IC3949 is the one jellyfish galaxy in our sample with both resolved optical spectroscopy from MaNGA and public, resolved molecular gas observations taken by the Atacama Large Millimeter/submillimeter Array (ALMA). For IC3949, this allows us to not only explore the star formation activity relative to the RPS tail but also probe the molecular gas density and depletion time as a function of position within this galaxy. IC3949 was observed in CO $J = 1 - 0$ in 2018 (PI: Lin; 2017.1.01093.S) and in HCN/HCO$^+$ in 2020 (PI: Lin; 2019.1.01178.S) as part of the larger ALMA MaNGA Quenching and Star Formation Survey (ALMaQUEST; Lin et al. 2020). Below we use these ALMA data to explore the molecular gas morphology in IC3949, in particular in the context of the region on enhanced star formation observed on the leading side of the galaxy.

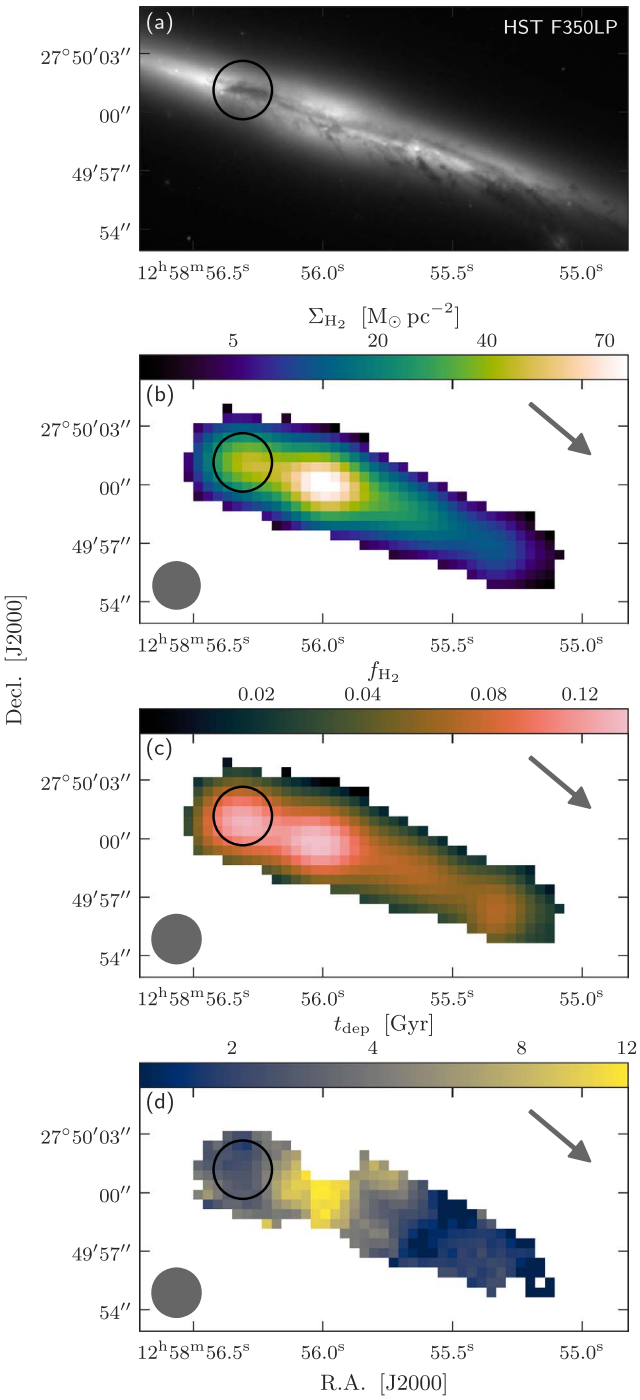

Figure 7. Maps of molecular gas and star formation properties in IC3949. From top to bottom: Hubble Space Telescope near-UV (F350LP), H_2 surface density, H_2 gas fraction ($\Sigma_{H_2}/\Sigma_\star$), and H_2 depletion time ($\Sigma_{H_2}/\Sigma_{SFR}$). The arrow in each panel shows the orientation of the observed RPS tail and the filled circle shows the FWHM resolution for the ALMA/MaNGA products. As a visual guide we also highlight the leading side region of enhanced star formation in each panel with the open circle. The HST data used in this figure can be found in MAST at: DOI: 10.17909/7ftv-0w17.

4.1. Bulk Molecular Gas Distribution

In this section we analyze the bulk molecular gas distribution in IC3949, as traced by CO $J = 1 - 0$ emission. We use CO products that were reduced and imaged by the ALMaQUEST team. Here we provide a description of the key components of this data processing; for a more detailed outline of the ALMaQUEST reduction procedure, please see Lin et al. (2020). IC3949 was observed in the C43-2 configuration of the ALMA 12 m array with an on-source integration time of ~22 min. The data were calibrated using Common Astronomy Software Applications (CASA) v5.4 (McMullin et al. 2007)

and the standard ALMA pipeline. The continuum was subtracted from the visibilities and CLEAN was used to clean the continuum-subtracted data down to 1σ. A Briggs' weighting with a robust parameter of 0.5 was used for the imaging. In order to match the pixel scale and the typical resolution of MaNGA data products, a user-specified pixel size of $0\farcs$ and a restoring beam size of $2\farcs$ FWHM were set. The resulting spectral line cube for CO $J = 1 - 0$ has a velocity channel width of $\sim$11 km s^{-1} and an rms of 0.6 mJy beam^{-1}. A CO moment-zero map for IC3949 was produced with `immoments` in CASA including only velocity channels where CO emission is present. We estimate the rms noise from source-free regions in the CO moment-zero map and any pixels with S/N < 3 are masked. The CO moment-zero map is converted to an H_2 surface density by adopting a constant conversion factor of $\alpha_{CO} = 4.35\ M_\odot\ (K\ km\ s^{-1}\ pc^{-2})^{-1}$ (e.g., Bolatto et al. 2013); this map is shown in Figure 7(b). In Figure 7 we also show maps of H_2 gas fraction and depletion time that are obtained by dividing the H_2 surface density map by the stellar mass and SFR surface density maps, respectively (see Figure 1 for the $\Sigma_\star$ and Σ_{SFR} maps for IC3949). In each panel we show an arrow denoting the projected orientation of the observed radio continuum tail and an open circle highlighting the region of enhanced star formation on the LH.

Relative to the galaxy center, the molecular gas disk of IC3949 is clearly asymmetric, being truncated on the LH of the galaxy (opposite to the tail direction) and more extended along the TH. This can likely be attributed to RPS which is transporting gas from the leading side of IC3949 "downstream" along the direction of the stripped tail. This ALMA observation does not detect any molecular gas in the stripped tail itself, as has been seen previously for some jellyfish galaxies (Jáchym et al. 2014, 2017, 2019; Moretti et al. 2020a, 2020b). Though it is worth noting that the observational setup was designed for observing molecular gas in the disk, therefore the primary beam response is substantially lower in the tail region beyond the optical extent of the galaxy. Forthcoming CO $J = 2 - 1$ observations of IC3949 from the ALMA-JELLY survey (PI: Jáchym; 2021.1.01616.L) will place stronger constraints on the presence, or lack thereof, of molecular gas in the RPS tail of IC3949. There is molecular gas asymmetry in the disk of IC3949, not just in terms of extent but also in terms of H_2 surface density. The H_2 surface density surface density is larger on the leading side of the disk (at fixed galactocentric radius), coincident with the enhanced star formation seen on the LH. This enhanced CO emission is subtle in the moment-zero map (Figure 7(a)) but more clearly visible in both the H_2 gas fraction map (Figure 7(b)) and the position–velocity diagram (PVD) shown in Figure 8. This enhanced H_2 surface density is consistent with a framework where ram pressure compresses gas on the leading side of galaxies, in turn catalyzing increased star formation (e.g., Gavazzi et al. 2001; Cramer et al. 2020; Boselli et al. 2021; Cramer et al. 2021; Roberts et al. 2022a). The PVD also shows a faint collection of extraplanar gas located at an offset of $\sim 10''$ along the trailing side of the galaxy. This gas is detached from the CO rotation curve and is potentially indicative of a plume of molecular gas being directly stripped from the disk of IC3949.

The depletion time is not constant across the disk of IC3949 (see Figure 7(c)) but instead is longest at the galaxy center and decreases radially outwards, ranging between 1 Gyr and 11 Gyr. Previous studies have found a mixture of enhanced or

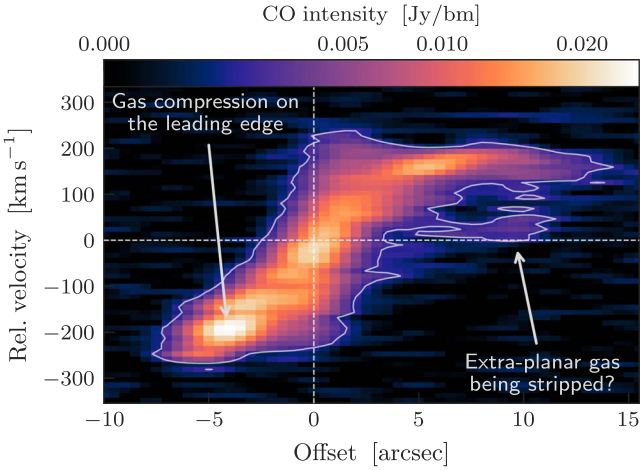

Figure 8. Position–velocity diagram (PVD) for IC3949 measured along the direction of the major axis (which roughly corresponds to the direction of the stripped tail). The width of the PVD box encompasses all of the CO emission shown in Figure 7. The gray contour corresponds to 3× rms of the CO cube.

suppressed depletion times in the centers of late-type galaxies, with the origin of these variations still being debated (e.g., Utomo et al. 2017; Colombo et al. 2018; Chown et al. 2019). Utomo et al. (2017) find, on average, shorter central gas depletion times in the EDGE-CALIFA sample of galaxies and argue that gas compression from a higher central stellar potential may shorten the depletion time. In contrast to this, Chown et al. (2019) find that it is primarily barred galaxies in the EDGE-CALIFA sample that have shorter central depletion times, while unbarred galaxies appear to have longer depletion times relative to their disks. In the center of IC3949, star formation appears suppressed relative to the molecular gas content, despite appearing to have a higher gas surface density. It is unclear what drives this suppression, but one explanation could be turbulence (e.g., Salas et al. 2021) that is potentially connected to the ongoing RPS. The spaxels within the galaxy center of IC3949 are classified as "composite" according to the resolved Baldwin, Phillips, & Terlevich diagram from MaNGA, thus it is possible that low-level AGN activity is contributing to the Hα flux in this region. This, however, will not resolve the difference between the central depletion time relative to the rest of the galaxy as this would actually imply that we are overestimating the central SFR and thus underestimating the depletion time. Finally, it is important to note that there is some evidence that α_{CO} is lower in galaxy centers (e.g., Sandstrom et al. 2013), which in turn would decrease the observed central depletion time. Over the region of enhanced star formation on the LH of IC3949 (circular aperture shown in Figure 7) the average depletion time is 2.7 Gyr, identical to the median value over the whole galaxy. Thus the enhanced star formation does not result from a high star formation efficiency (SFE) but instead an increase in molecular gas that is in line with the resolved Kennicutt–Schmidt (rKS; Schmidt 1959; Kennicutt 1998b) relation for IC3949.

4.2. Dense Molecular Gas Distribution

For a subset of ALMaQUEST galaxies, including IC3949, follow-up observations of the $J = 1 - 0$ transitions for the dense gas molecular tracers HCN and HCO^+ were obtained in ALMA Cycle 7. HCN and HCO^+ have critical densities of $\sim 10^5$ cm^{-3} and $\sim 5 \times 10^4$ cm^{-3} (Shirley 2015), respectively,

compared to $\sim 10^3\,\mathrm{cm}^{-3}$ for CO, and thus trace a denser component of the ISM. Here we describe and present the imaging of the HCN and HCO^+ lines for IC3949. A full analysis of the five ALMaQUEST galaxies with dense gas observations will be presented in a forthcoming paper (L. Lin et al. 2022, in preparation).

Dense gas observations at 88.631 GHz (PI: Li; 2019.1.01178.S) were carried out with ALMA in Cycle 7 using the Band 3 receiver and C43-2 configuration. These observations cover the full FOV of the CO $J = 1 - 0$ observations described in the previous section. The spectral setup includes one line targeting HCN $J = 1 - 0$ and three low-resolution spectral windows for the continuum. The line spectral window has a bandwidth of $\sim$930 MHz (3200 $\mathrm{km\,s}^{-1}$), with a native channel width of $\sim 2\,\mathrm{km\,s}^{-1}$, and is sufficiently wide to also include the HCO^+ $J = 1 - 0$ line (89.189 GHz). The data were processed by the standard pipeline in CASA 5.6. Continuum is subtracted from the data in the visibility domain. The task `tclean` was employed for deconvolution with a Briggs' robustness parameter of 0.5. We adopted a user-specified image center, pixel size (0.″5), and restoring beam size (2.″5) to match the image grid and the spatial resolution of the MaNGA images. The restoring beam size is similar to that of the native beam size reported by the `tclean` (2.″7 × 2.″4). The HCN and HCO^+ lines were imaged separately, and to increase the S/N the spectral channels are binned to $\sim 50\,\mathrm{km\,s}^{-1}$. The rms noise of the spectral line data cubes are 0.13 mJy beam^{-1} and 0.14 mJy beam^{-1} for HCN and HCO^+, respectively. The integrated intensity maps of HCN and HCO^+ were constructed using the task `immoments` in CASA by integrating emission from a velocity range set by hand to match the observed line profile without any clipping in signal.

In Figure 9 we show integrated intensity (moment-zero) maps of HCN and HCO^+ for IC3949. We also show the outline of the detected CO emission from Figure 7(a) with the solid contour and the galaxy center with the cross. Emission in the moment-zero maps (for both HCN and HCO^+) is restricted to the galaxy center and the LH of IC3949, with no significant emission detected on the TH. The fact that emission from these dense gas tracers is only detected along the leading side is additional evidence for gas compression from ram pressure, as was argued for in Section 4.1. There are also morphological differences between HCN and HCO^+ in Figure 9. HCN emission peaks at the galaxy center and decreases radially toward the leading edge of the galaxy, whereas HCO^+ emission is bimodal with a peak at the galaxy center and a second peak that is spatially coincident with the region of enhanced star formation on the LH. We also measure the intensity ratio between dense gas tracers and CO, $I_{\mathrm{dense}}/I_{\mathrm{CO}}$, where $I_{\mathrm{dense}} = I_{\mathrm{HCN}}$ or $I_{\mathrm{dense}} = I_{\mathrm{HCO^+}}$, and the HCN-to-$HCO^+$ ratio ($I_{\mathrm{HCN}}/I_{\mathrm{HCO^+}}$) in three rectangular apertures that span the detected dense gas emission in the moment-zero maps (see Figure 9). These apertures are oriented along the major axis of IC3949, are spaced in intervals of 2.″5, i.e., one beam's width, and cover the area between the galaxy center ($d_{\mathrm{maj}} = 0''$ in Figure 10) and the region of enhanced star formation on the leading edge of IC3949 ($d_{\mathrm{maj}} = 5''$ in Figure 10). We color the data points in Figure 10 by the average sSFR in each aperture in order to further emphasize the increase in star formation toward the leading edge. As shown in Figure 10(a), the dense gas fraction traced by HCO^+ increases monotonically toward the region of enhanced star formation on the leading side,

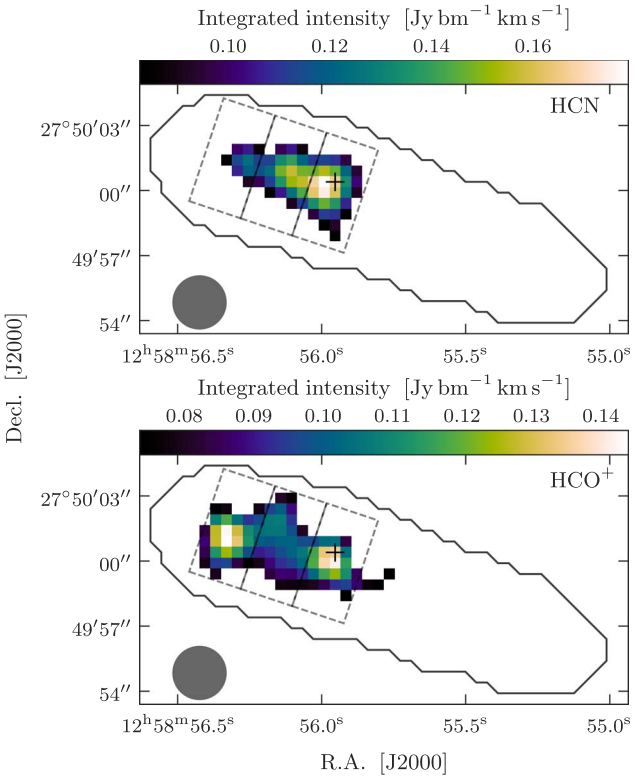

Figure 9. Integrated intensity maps of HCN and HCO^+ for IC3949. The solid contour shows the extent of the CO emission in IC3949, the cross marks the optical galaxy center, and the filled circle shows the FWHM beam size.

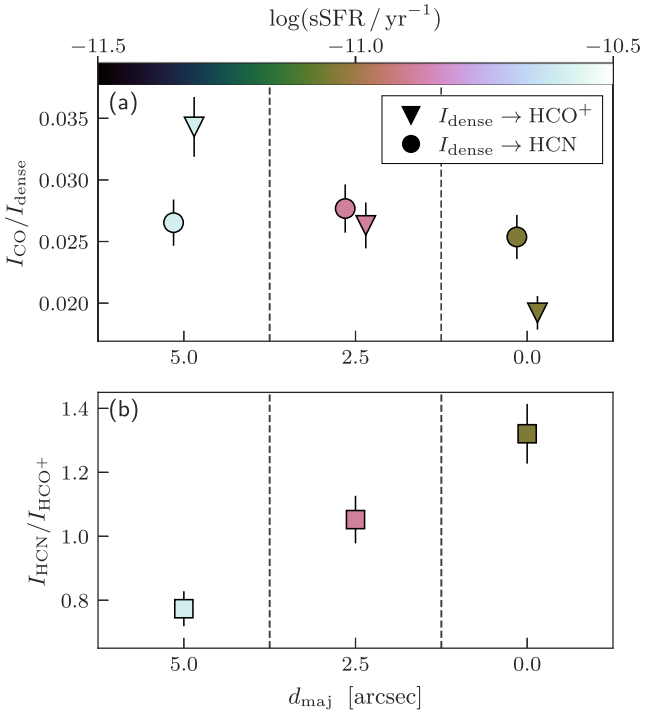

Figure 10. Top: dense gas fraction ($I_{\mathrm{dense}}/I_{\mathrm{CO}}$) derived from HCN (circles) and HCO^+ (triangles) within the three apertures shown in Figure 9. The *x*-axis, d_{maj}, corresponds to the distance of the aperture center along the galaxy major axis (in the direction of the leading edge). Bottom: HCN-HCO^+ line ratio within the three apertures shown in Figure 9. In both panels the data points are colored by the average sSFR in each aperture and the error bars are a combination of random error derived from bootstrap resampling and a 5% calibration uncertainty assumed for each line flux (ALMA Band 3; ALMA Technical Handbook).

whereas the dense gas fraction traced by HCN remains constant across all three apertures. These differences between HCN and HCO^+ are further illustrated in Figure 10(b), where we plot the HCN-to-HCO^+ ratio measured in each of the three apertures. This ratio is largest at the galaxy center and decreases monotonically toward the region of enhanced star formation on the leading side, where HCO^+ becomes brighter than HCN and the ratio falls below unity. Previous works have found that low HCN-HCO^+ ratios are typically associated with starburst regions in galaxies (e.g., Kohno et al. 2001; Meijerink et al. 2007; Privon et al. 2015; Bemis & Wilson 2019; Butterworth et al. 2022; Zhou et al. 2022). This is likely due to an increase in HCO^+ abundance driven by the enhanced UV radiation fields and cosmic ray ionization expected in regions of strong star formation (e.g., Krips et al. 2008; Meijerink et al. 2011; Nayana et al. 2020). Our resolved observations of the HCN-to-HCO^+ ratio in IC3949 supports such a picture as the region of enhanced star formation on the leading side is characterized by a particularly low HCN-to-HCO^+ ratio. Though we also note that HCO^+ has a lower critical density than HCN (e.g., Shirley 2015), thus the HCN-HCO^+ ratio may be decreasing away from the galaxy center, in part, due to a decreasing average density of molecular gas.

5. Discussion and Conclusions

In this work we use MaNGA IFS observations to present evidence for enhanced star formation on the LH for a sample of 29 jellyfish galaxies. This highlights a key phase experienced by galaxies undergoing RPS where ram pressure is capable of enhancing star formation prior to quenching. Thus the SFR does not necessarily decrease monotonically through the environmental quenching process. The fact that this SFR enhancement is connected to the orientation of the stripped tail (see Figures 3, 5) lends further credence to this enhancement being connected to gas compression from ram pressure. This is in line with the compression that is apparent in the LOFAR radio emission where steep surface brightness gradients (i.e., closely spaced contour levels) are visible on the leading edges for many of these jellyfish galaxies (see Figure 1). The results from this work are in agreement with previous observational studies that have demonstrated enhanced star formation on the leading edge of select galaxies undergoing RPS (Gavazzi et al. 2001; Boselli et al. 2021; Roberts et al. 2022a; Hess et al. 2022) as well as the results from the EAGLE hydrodynamical simulation by Troncoso-Iribarren et al. (2020). Additionally, Vulcani et al. (2020) find evidence for enhanced star formation at all galactocentric radii within the disks of galaxies undergoing RPS from the GAs Stripping Phenomena in galaxies sample. More broadly this work is also consistent with the fact that, on a population level, galaxies undergoing RPS have integrated SFRs that are sytematically enhanced (e.g., Dressler & Gunn 1983; Ebeling et al. 2014; Vulcani et al. 2018; Roberts & Parker 2020; Vulcani et al. 2020; Wang et al. 2020; Roberts et al. 2021b; Durret et al. 2021; Lee et al. 2022c). Based on the results of this work it is likely that these enhanced integrated SFRs are being primarily driven by star formation activity on the leading side. This work presents the largest sample of galaxies for which ram-pressure-enhanced star formation has been resolved and studied, though this may be extended in the near future. Upon completion of the Canada-France Imaging Survey (Ibata et al. 2017), deep, high-resolution *u*-band imaging will be available as a resolved SFR tracer for the entire sample of ∼150 LOFAR jellyfish galaxies from Roberts et al. (2021a, 2021b), expanding the sample size relative to this work by a factor of ∼5.

In Section 4 we present a case study on the distribution of molecular gas for one jellyfish galaxy, IC3949, in our sample. For IC3949 there is evidence for an increase in molecular gas density over the observed region of enhanced star formation on the LH. The relationship between H_2 surface density and SFR in this region follows the expectation from the rKS relation for IC3949, suggesting that the enhanced star formation is a result of an increase in molecular gas (likely due to compression from ram pressure) and not an increase in SFE. We note that Tomičić et al. (2018) present evidence for short depletion times (high SFE) on the leading side of the nearby group galaxy NGC2276 that is undergoing RPS (and also likely a tidal interaction with NGC2300). NGC2276 is a starburst galaxy ($SFR \approx 10-20\,M_\odot\,yr^{-1}$; Kennicutt 1983; Wolter et al. 2015; Tomičić et al. 2018), whereas IC3949 is in the green valley at an advanced quenching stage ($SFR \approx 0.7\,M_\odot\,yr^{-1}$; Salim et al. 2016, 2018), thus this difference may reflect the very different stages of star formation for these two galaxies. Villanueva et al. (2022) study a sample of 38 Virgo galaxies from the VERTICO survey (Brown et al. 2021) and find that the SFE within the effective radius decreases and the molecular-to-atomic gas ratio increases with increasing environmental perturbation (as traced by H I). They attribute this to environmental effects that remove atomic gas from galaxies, drive molecular gas to the central regions of galaxies, and/or promote the conversion from atomic to molecular gas. The median SFE of $3.7 \times 10^{-10}\,yr^{-1}$ ($t_{dep} = 2.7$ Gyr) that we measure for IC3949 is consistent with the range of values that Villanueva et al. (2022) find for Virgo galaxies with perturbed H I morphologies. There is further observational evidence for ram pressure promoting the formation of molecular gas (e.g., Moretti et al. 2020a, 2020b), and in particular driving enhanced molecular gas densities along the leading edge of galaxies undergoing RPS (e.g., Lee et al. 2017; Cramer et al. 2020, 2021). The enhanced H_2 density that we show in Figure 8 appears similar to the region of gas compression that Cramer et al. (2020) highlight in the PVD for the Virgo cluster galaxy NGC4402. Additionally, the dense molecular gas tracers HCN and HCO^+ are only detected in IC3949 over a region from the galaxy center along the leading side—not on the TH of the galaxy. This reinforces the notion that there are increased ISM densities on the LH. To our best knowledge, Section 4.2 is the first ever analysis of the distribution of *dense* molecular gas in a jellyfish galaxy undergoing RPS. Moving forward, dense gas observations will hopefully be obtained for more galaxies undergoing RPS in order to elucidate whether the signatures observed for IC3949 are typical or not.

5.1. Summary

In this work we present clear evidence for an enhancement of star formation on the LH of galaxies undergoing RPS. This star formation enhancement is consistent with predictions from hydrodynamical simulations and is likely driven by gas compression via ram pressure. Below we highlight the main scientific conclusions from this work.

1. Jellyfish galaxies show enhanced SFRs and sSFRs on the LH of the galaxy, opposite to the direction of the stripped tail (Figure 3).

2. The dividing line that maximizes the star formation anisotropy for each jellyfish galaxy is systematically aligned with the dividing line between the leading and trailing halves of the galaxy as inferred from the observed tail direction (Figure 5).
3. For the jellyfish galaxies in our sample, the locations of the maximum sSFR are preferentially found on the LH of the galaxy (Figure 6).
4. The jellyfish galaxy IC3949 has an area of enhanced molecular gas surface density on the leading side of the galaxy that is spatially coincident with the observed star formation enhancement. This region has a typical H_2 depletion time (as traced by CO) compared to the rest of the galaxy, suggesting that the enhancement star formation is driven by an increase in molecular gas and not an abnormally high SFE (Figures 7 and 8).
5. In IC3949, emission from dense molecular gas tracers HCN and HCO^+ is only detected between the galaxy center and the leading edge, reinforcing the increase in ISM density on the leading side (Figure 9).

Recent and forthcoming ALMA large programs such as VERTICO (Brown et al. 2021) and ALMA-JELLY (PI: Jáchym; 2021.1.01616.L) will significantly increase the number of galaxies undergoing RPS with resolved CO observations and thus shed further light on the relationship between molecular gas and star formation in such systems. We find evidence for ram pressure compression of the ISM in IC3949, but it is still not clear whether this is a generic feature of all galaxies undergoing RPS. These large CO surveys will take a large step toward addressing this open question and will also provide a parent sample from which compelling targets can be selected for follow-up observations of dense gas tracers and/or CO at higher spatial resolution. For a more complete understanding of the impact of RPS on star formation and molecular gas, probing the ISM at cloud scales in jellyfish galaxies should be a priority, moving forward.

We thank the Leiden/ESA Astrophysics Program for Summer Students for hosting D.T. while working on this project. I. D.R. and R.J.v.W. acknowledge support from the ERC Starting Grant Cluster Web 804208. L.L. acknowledges support from the Academia Sinica under the Career Development Award CDA107-M03 and the Ministry of Science and Technology of Taiwan under the grant No. MOST 111-2112-M-001-044. H.A.P. acknowledges support from the National Science and Technology Council of Taiwan under grant No. 110-2112-M-032-020-MY3. A.I. acknowledges the INAF founding program "Ricerca Fondamentale 2022" (PI A. Ignesti).

Funding for the Sloan Digital Sky Survey IV has been provided by the Alfred P. Sloan Foundation, the U.S. Department of Energy Office of Science, and the Participating Institutions. SDSS-IV acknowledges support and resources from the Center for High Performance Computing at the University of Utah. The SDSS website is www.sdss.org. SDSS-IV is managed by the Astrophysical Research Consortium for the Participating Institutions of the SDSS Collaboration including the Brazilian Participation Group, the Carnegie Institution for Science, Carnegie Mellon University, Center for Astrophysics —Harvard & Smithsonian, the Chilean Participation Group, the French Participation Group, Instituto de Astrofísica de Canarias, The Johns Hopkins University, Kavli Institute for the Physics and Mathematics of the Universe (IPMU)/University of Tokyo, the Korean Participation Group, Lawrence Berkeley National Laboratory, Leibniz Institut für Astrophysik Potsdam (AIP), Max-Planck-Institut für Astronomie (MPIA Heidelberg), Max-Planck-Institut für Astrophysik (MPA Garching), Max-Planck-Institut für Extraterrestrische Physik (MPE), National Astronomical Observatories of China, New Mexico State University, New York University, University of Notre Dame, Observatário Nacional / MCTI, The Ohio State University, Pennsylvania State University, Shanghai Astronomical Observatory, United Kingdom Participation Group, Universidad Nacional Autónoma de México, University of Arizona, University of Colorado Boulder, University of Oxford, University of Portsmouth, University of Utah, University of Virginia, University of Washington, University of Wisconsin, Vanderbilt University, and Yale University.

This paper makes use of the following ALMA data: ADS/JAO.ALMA#2017.1.01093.S, ADS/JAO.ALMA#2019.1.01178.S. ALMA is a partnership of ESO (representing its member states), the NSF (USA), and NINS (Japan), together with NRC (Canada), MOST and ASIAA (Taiwan), and KASI (Republic of Korea), in cooperation with the Republic of Chile. The Joint ALMA Observatory is operated by ESO, AUI/NRAO and NAOJ. In addition, publications from NA authors must include the standard NRAO acknowledgement: The National Radio Astronomy Observatory is a facility of the National Science Foundation operated under cooperative agreement by Associated Universities, Inc.

Software: ASTROPY (Robitaille et al. 2013), CASA (McMullin et al. 2007), CMASHER (van der Velden 2020), DS9 (Joye & Mandel 2003), MARVIN (Cherinka et al. 2019), MATPLOTLIB (Hunter 2007), NUMPY (Harris et al. 2020), PHOTUTILS (Bradley et al. 2022), RSMF (https://rsmf.readthedocs.io/en/latest/source/howto.html), SCIPY (Virtanen et al. 2020), SPECTRAL-CUBE (https://spectral-cube.readthedocs.io/en/latest/).

ORCID iDs

Ian D. Roberts https://orcid.org/0000-0002-0692-0911
Ashley R. Bemis https://orcid.org/0000-0003-0618-8473
Sara L. Ellison https://orcid.org/0000-0002-1768-1899
Lihwai Lin https://orcid.org/0000-0001-7218-7407
Hsi-An Pan https://orcid.org/0000-0002-1370-6964
Alessandro Ignesti https://orcid.org/0000-0003-1581-0092
Sarah Leslie https://orcid.org/0000-0002-4826-8642
Reinout J. van Weeren https://orcid.org/0000-0002-0587-1660

References

Abdurro'uf, Accetta, K., Aerts, C., et al. 2022, ApJS, 259, 35
Baldwin, J. A., Phillips, M. M., & Terlevich, R. 1981, PASP, 93, 5
Bemis, A., & Wilson, C. D. 2019, AJ, 157, 131
Boissier, S., Boselli, A., Duc, P. A., et al. 2012, A&A, 545, A142
Bolatto, A. D., Wolfire, M., & Leroy, A. K. 2013, AR&AA, 51, 207
Boselli, A., Fossati, M., Ferrarese, L., et al. 2018, A&A, 614, A56
Boselli, A., Fossati, M., & Sun, M. 2022, A&ARv, 30, 3
Boselli, A., Lupi, A., Epinat, B., et al. 2021, A&A, 646, A139
Bradley, L., Sipocz, B., Robitaille, T., et al. 2022, astropy/photutils: v1.5.0, Zenodo, doi:10.5281/zenodo.6825092
Brown, T., Catinella, B., Cortese, L., et al. 2017, MNRAS, 466, 1275
Brown, T., Wilson, C. D., Zabel, N., et al. 2021, ApJS, 257, 21
Bundy, K., Bershady, M. A., Law, D. R., et al. 2015, ApJ, 798, 7
Butterworth, J., Holdship, J., Viti, S., & García-Burillo, S. 2022, A&A, 667, A131
Chen, H., Sun, M., Yagi, M., et al. 2020, MNRAS, 496, 4654
Cherinka, B., Andrews, B. H., Sánchez-Gallego, J., et al. 2019, AJ, 158, 74
Chown, R., Li, C., Athanassoula, E., et al. 2019, MNRAS, 484, 5192

Chung, A., van Gorkom, J. H., Kenney, J. D. P., Crowl, H., & Vollmer, B. 2009, AJ, 138, 1741
Chung, A., van Gorkom, J. H., Kenney, J. D. P., & Vollmer, B. 2007, ApJL, 659, L115
Cid Fernandes, R., Pérez, E., Garcıa Benito, R., et al. 2013, A&A, 557, A86
Ciocan, B. I., Maier, C., Ziegler, B. L., & Verdugo, M. 2020, A&A, 633, A139
Colombo, D., Kalinova, V., Utomo, D., et al. 2018, MNRAS, 475, 1791
Cortese, L., Catinella, B., & Smith, R. 2021, PASA, 38, e035
Cowie, L. L., & Songaila, A. 1977, Natur, 266, 501
Cramer, W. J, Kenney, J. D. P, Cortes, J. R, et al. 2020, ApJ, 901, 95
Cramer, W. J., Kenney, J. D. P., Tonnesen, S., et al. 2021, ApJ, 921, 22
Cramer, W. J., Noble, A. G., Massingill, K., et al. 2022, arXiv:2209.06929
Croton, D. J., Farrar, G. R., Norberg, P., et al. 2005, MNRAS, 356, 1155
Davies, L. J. M., Robotham, A. S. G., Lagos, C. D. P., et al. 2019, MNRAS, 483, 5444
Dressler, A. 1980, ApJ, 236, 351
Dressler, A., & Gunn, J. E. 1983, ApJ, 270, 7
Durret, F., Chiche, S., Lobo, C., & Jauzac, M. 2021, A&A, 648, A63
Ebeling, H., Stephenson, L. N., & Edge, A. C. 2014, ApJL, 781, L40
Gavazzi, G., Boselli, A., Mayer, L., et al. 2001, ApJL, 563, L23
Gavazzi, G., & Jaffe, W. 1987, A&A, 186, L1
George, K., Poggianti, B. M., Gullieuszik, M., et al. 2018, MNRAS, 479, 4126
Gunn, J. E., & Gott, J. R., III 1972, ApJ, 176, 1
Harris, C. R., Millman, K. J., van der Walt, S. J., et al. 2020, Natur, 585, 357
Hess, K. M., Kotulla, R., Chen, H., et al. 2022, arXiv:2209.05605
Hunter, J. D. 2007, CSE, 9, 90
Ibata, R. A., McConnachie, A., Cuilland re, J.-C., et al. 2017, ApJ, 848, 128
Jáchym, P., Combes, F., Cortese, L., Sun, M., & Kenney, J. D. P. 2014, ApJ, 792, 11
Jáchym, P., Kenney, J. D. P., Sun, M., et al. 2019, ApJ, 883, 145
Jáchym, P., Sun, M., Kenney, J. D. P., et al. 2017, ApJ, 839, 114
Jaffé, Y. L., Poggianti, B. M., Moretti, A., et al. 2018, MNRAS, 476, 4753
Jian, H.-Y., Lin, L., & Chiueh, T. 2012, ApJ, 754, 26
Jian, H.-Y., Lin, L., Oguri, M., et al. 2018, PASJ, 70, S23
Joye, W. A., & Mandel, E. 2003, in ASP Conf. Ser. 295, Astronomical Data Analysis Software and Systems XII, ed. H. E. Payne, R. I. Jedrzejewski, & R. N. Hook (San Francisco, CA: ASP), 489
Kauffmann, G., Heckman, T. M., Tremonti, C., et al. 2003, MNRAS, 346, 1055
Kenney, J. D. P., Abramson, A., & Bravo-Alfaro, H. 2015, AJ, 150, 59
Kenney, J. D. P., van Gorkom, J. H., & Vollmer, B. 2004, AJ, 127, 3361
Kennicutt, R. C., Jr. 1998a, ARA&A, 36, 189
Kennicutt, R. C., Jr. 1983, ApJ, 272, 54
Kennicutt, R. C., Jr. 1998b, ApJ, 498, 541
Kewley, L. J., Dopita, M. A., Sutherland, R. S., Heisler, C. A., & Trevena, J. 2001, ApJ, 556, 121
Kewley, L. J., Groves, B., Kauffmann, G., & Heckman, T. 2006, MNRAS, 372, 961
Kimm, T., Somerville, R. S., Yi, S. K., et al. 2009, MNRAS, 394, 1131
Kohno, K., Matsushita, S., Vila-Vilaró, B., et al. 2001, in ASP Conf. Ser. 249, The Central Kiloparsec of Starbursts and AGN: The La Palma Connection, ed. J. H. Knapen et al. (San Francisco, CA: ASP), 672
Krips, M., Neri, R., García-Burillo, S., et al. 2008, ApJ, 677, 262
Lacerda, E. A. D., Sánchez, S. F., Mejía-Narváez, A., et al. 2022, NewA, 97, 101895
Lal, D. V., Lyskova, N., Zhang, C., et al. 2022, ApJ, 934, 170
Larson, R. B., Tinsley, B. M., & Caldwell, C. N. 1980, ApJ, 237, 692
Lee, B., & Chung, A. 2018, ApJL, 866, L10
Lee, B., Chung, A., Tonnesen, S., et al. 2017, MNRAS, 466, 1382
Lee, B., Wang, J., Chung, A., et al. 2022a, ApJS, 262, 31
Lee, J. H., Lee, M. G., Mun, J. Y., Cho, B. S., & Kang, J. 2022b, ApJ, 940, 24
Lee, J. H., Lee, M. G., Mun, J. Y., Cho, B. S., & Kang, J. 2022c, ApJL, 931, L22
Lee, M. G., & Jang, I. S. 2016, ApJ, 819, 77
Lim, S. H., Mo, H. J., Lu, Y., Wang, H., & Yang, X. 2017, MNRAS, 470, 2982
Lin, L., Ellison, S. L., Pan, H.-A., et al. 2020, ApJ, 903, 145
Lin, L., Jian, H.-Y., Foucaud, S., et al. 2014, ApJ, 782, 33
Mahajan, S., Singh, K. P., Postma, J. E., et al. 2022, PASA, 39, e048
Maier, C., Hayashi, M., Ziegler, B. L., & Kodama, T. 2019, A&A, 626, A14
Mayer, L., Mastropietro, C., Wadsley, J., Stadel, J., & Moore, B. 2006, MNRAS, 369, 1021
McMullin, J. P., Waters, B., Schiebel, D., Young, W., & Golap, K. 2007, in ASP Conf. Ser. 376, Astronomical Data Analysis Software and Systems XVI, ed. R. A. Shaw, F. Hill, & D. J. Bell (San Francisco, CA: ASP), 127
Meijerink, R., Spaans, M., & Israel, F. P. 2007, A&A, 461, 793
Meijerink, R., Spaans, M., Loenen, A. F., & van der Werf, P. P. 2011, A&A, 525, A119
Moon, J.-S., An, S.-H., & Yoon, S.-J. 2019, ApJ, 882, 14
Moore, B., Katz, N., Lake, G., Dressler, A., & Oemler, A. 1996, Natur, 379, 613
Moretti, A., Paladino, R., Poggianti, B. M., et al. 2020a, ApJ, 889, 9
Moretti, A., Paladino, R., Poggianti, B. M., et al. 2020b, ApJL, 897, L30
Murphy, E. J., Kenney, J. D. P., Helou, G., Chung, A., & Howell, J. H. 2009, ApJ, 694, 1435
Nayana, A. J., Naslim, N., Onishi, T., et al. 2020, ApJ, 902, 140
Nulsen, P. E. J. 1982, MNRAS, 198, 1007
Oosterloo, T., & van Gorkom, J. 2005, A&A, 437, L19
Peng, Y., Maiolino, R., & Cochrane, R. 2015, Natur, 521, 192
Peng, Y.-j., Lilly, S. J., Kovač, K., et al. 2010, ApJ, 721, 193
Poggianti, B. M., Ignesti, A., Gitti, M., et al. 2019, ApJ, 887, 155
Poggianti, B. M., Moretti, A., Gullieuszik, M., et al. 2017, ApJ, 844, 48
Postman, M., & Geller, M. J. 1984, ApJ, 281, 95
Privon, G. C., Herrero-Illana, R., Evans, A. S., et al. 2015, ApJ, 814, 39
Quilis, V., Moore, B., & Bower, R. 2000, Sci, 288, 1617
Roberts, I. D., & Parker, L. C. 2020, MNRAS, 495, 554
Roberts, I. D., Parker, L. C., Brown, T., et al. 2019, ApJ, 873, 42
Roberts, I. D., Parker, L. C., Gwyn, S., et al. 2022b, MNRAS, 509, 1342
Roberts, I. D., van Weeren, R. J., McGee, S. L., et al. 2021a, A&A, 652, A153
Roberts, I. D., van Weeren, R. J., McGee, S. L., et al. 2021b, A&A, 650, A111
Roberts, I. D., van Weeren, R. J., Timmerman, R., et al. 2022a, A&A, 658, A44
Robitaille, T. P., Tollerud, E. J., Greenfield, P., et al. 2013, A&A, 558, A33
Salas, J. M., Morris, M. R., & Naoz, S. 2021, AJ, 161, 243
Salim, S., Boquien, M., & Lee, J. C. 2018, ApJ, 859, 11
Salim, S., Lee, J. C., Janowiecki, S., et al. 2016, ApJS, 227, 2
Salpeter, E. E. 1955, ApJ, 121, 161
Sánchez, S. F., Pérez., E., Sánchez-Blá zquez, P., et al. 2016a, RMxAA, 52, 21
Sánchez, S. F., Pérez, E., Sánchez-Blázquez, P., et al. 2016b, RMxAA, 52, 171
Sandstrom, K. M., Leroy, A. K., Walter, F., et al. 2013, ApJ, 777, 5
Schaye, J., Crain, R. A., Bower, R. G., et al. 2015, MNRAS, 446, 521
Schmidt, M. 1959, ApJ, 129, 243
Scholz, F. W., & Stephens, M. A. 1987, J. Am. Stat. Assoc., 82, 918
Schulz, S., & Struck, C. 2001, MNRAS, 328, 185
Shimwell, T. W., Hardcastle, M. J., Tasse, C., et al. 2022, A&A, 659, A1
Shirley, Y. L. 2015, PASP, 127, 299
Smith, R. J., Lucey, J. R., Hammer, D., et al. 2010, MNRAS, 408, 1417
Sun, M., Donahue, M., Roediger, E., et al. 2010, ApJ, 708, 946
Sun, M., Ge, C., Luo, R., et al. 2021, NatAs, 6, 270
Sun, M., Jones, C., Forman, W., et al. 2006, ApJL, 637, L81
Tomičić, N., Hughes, A., Kreckel, K., et al. 2018, ApJL, 869, L38
Troncoso-Iribarren, P., Padilla, N., Santander, C., et al. 2020, MNRAS, 497, 4145
Utomo, D., Bolatto, A. D., Wong, T., et al. 2017, ApJ, 849, 26
van der Velden, E. 2020, JOSS, 5, 2004
van Haarlem, M. P., Wise, M. W., Gunst, A. W., et al. 2013, A&A, 556, A2
Villanueva, V., Bolatto, A. D., Vogel, S., et al. 2022, arXiv:2210.05381
Virtanen, P., Gommers, R., Oliphant, T. E., et al. 2020, NatMe, 17, 261
Vogt, F. P. A., Dopita, M. A., & Kewley, L. J. 2013, ApJ, 768, 151
Vollmer, B., Soida, M., Braine, J., et al. 2012, A&A, 537, A143
Vulcani, B., Poggianti, B. M., Gullieuszik, M., et al. 2018, ApJL, 866, L25
Vulcani, B., Poggianti, B. M., Tonnesen, S., et al. 2020, ApJ, 899, 98
Wang, J., Xu, W., Lee, B., et al. 2020, ApJ, 903, 103
Wetzel, A. R., Tinker, J. L., & Conroy, C. 2012, MNRAS, 424, 232
Williams, W. L., Hardcastle, M. J., Best, P. N., et al. 2019, A&A, 622, A2
Wolter, A., Esposito, P., Mapelli, M., Pizzolato, F., & Ripamonti, E. 2015, MNRAS, 448, 781
Yagi, M., Yoshida, M., Komiyama, Y., et al. 2010, AJ, 140, 1814
Yang, Y., Ianjamasimanana, R., Hammer, F., et al. 2022, A&A, 660, L11
Yun, K., Pillepich, A., Zinger, E., et al. 2019, MNRAS, 483, 1042
Zabel, N., Brown, T., Wilson, C. D., et al. 2022, ApJ, 933, 10
Zhou, J., Zhang, Z.-Y., Gao, Y., et al. 2022, ApJ, 936, 58